Development of an automatic observation system for Fabry-Perot interferometers

Mamoru Ishii[1], Shoichi Okano[2], Eiichi Sagawa[1], Shin'ichi Watari[1],
Hirotaka Mori[1], Iwao Iwamoto[1], Kazumasa Kanda[3],
Fumihiko Kamimura[4] and Dai Sakamoto[4]

[1] *Communications Research Laboratory, Ministry of Posts and Telecommunications,*
Koganei-shi, Tokyo 184-8795
[2] *Tohoku University, Aoba-ku, Sendai 980-8587*
[3] *Shinwa Koki Inc., 5-16-6, Nisshin-cho, Fuchu-shi, Tokyo 183-0036*
[4] *A.D. Inc., 2-12-18 Sagamihara, Sagamihara 229-0031*

Abstract: The importance of automatic observation systems for ground-based optical instruments is increasing since clustered measurements are being made with only a few operators. We have developed an automatic observation system for use with both a scanning and an all-sky Fabry-Perot interferometer. This paper describes the optical system of the instrument, its performance when observing auroras, and the details of the automatic observation system. The S/N ratio of the observed fringe exceeds 500, even if the auroral activity is low. Using the Internet or telephone lines, an operator can monitor and control multiple optical instruments from a remote site. In addition, we introduce a new analysis software for estimating the emission intensity, wind velocity and temperature. Once the system is further improved by modifying it to enable radio communication, the construction of remote-controlled, relocatable observatories will become feasible, representing a remarkable evolution in optical measurement technology.

1. Introduction

The upper atmosphere emits a weak light both night and day as a result of photoionization, photodissociation by sunlight, and collisions between particles. This light, also known as airglow, has a specific wavelength spectrum. The mechanism by which aurora are generated in the polar regions is quite different from that of airglow, but aurora emissions also have specific wavelengths. High wavelength-resolution measurements of this light provide information on the velocity of air movement (wind) along the line of sight in terms of the difference between the anticipated and measured wavelengths, information regarding the temperature can be obtained by measuring the spectral widths of the emissions. To estimate wind velocities and temperatures, precise information on the intensity of each color (or wavelength) is necessary.

Optical observations using Fabry-Perot interferometers (FPIs) can be a very powerful approach for obtaining these precise spectrometries. The Fabry-Perot etalon is a combination of two optical flats placed in parallel with a space inbetween. When monochromatic light falls upon the etalon, the light undergoes a series of transmission

and reflections. The emerging rays produce an interference pattern, the bands of which are known as "fringes". The location of the peak and the width of the fringes contain information on the velocities and temperature, respectively, of the light emitting atmosphere.

The fundamental theory behind the use of this instrument was established about one hundred years ago (Fabry and Perot, 1896, 1897), and FPIs have been frequently used for airglow/aurora observations since the 1920s (Babcock, 1923). Despite such a long history, however, the importance of FPI observations continues to increase. Conventional FPIs have a narrow field of view (~ 1–2 degrees), and the region of observation must be scaned to deduce the spatial distribution of the thermosphere and the mesosphere (Burnside et al., 1981; Hernandez, 1982; Sipler et al., 1983; Meriwether et al., 1986; Biondi et al., 1988; Crickmore et al., 1991; Buonsanto et al., 1992; Aruliah and Rees, 1995; Smith and Hernandez, 1995; Innis et al., 1996, 1997). Rees and Greenaway (1983) developed an all-sky FPI using a fish-eye lens, which has a wide field of view (~ 160 degrees). This instrument can be used to produce a two-dimensional distribution of the neutral wind and temperature from one fringe image. Such a wide range of observation capabilities is one of the merits of passive optical measurements (Rees et al., 1984; Batten et al., 1988; Biondi et al., 1995; Nakajima et al., 1995; Conde and Smith, 1998; Ishii et al., 1999). Optical observations using FPIs installed onboard satellites have also been used to observe the spatial distribution of wind and temperature over large areas (Hays et al., 1984; Killeen and Roble, 1988; Killeen et al., 1988).

In spite of these revolutionary improvements, the observation area of ground-based FPIs is relatively small compared to that of satellite measurements. Recent studies, such as the investigation of neutral heating by aurora in the polar region (Walterscheid et al., 1985), require observations over a wide range and with a high time resolution. To solve these problems, an automatic observation system would be a powerful tool not only for satellite FPIs, but also for ground-based FPIs. Simultaneous observations from multiple observatories are necessary to cover a wide observation area. An automatic and remote control system is indispensable if a small number of operators (ultimately one person) are to manage multiple instruments at several remote sites. Such automated control systems have been described in a number of publications (Sipler et al., 1983; Meriwether et al., 1983, 1986).

This paper describes the all-sky and scanning FPIs with automatic/remote control systems that have been developed by the Communications Research Laboratory. The advantages of these optical instruments are (1) two different wavelength emissions can be measured using a dichroic mirror, and (2) a high time-resolution enabling a high-S/N-ratio image (exceeding 500 in 1–2 min for aurora; 5 min for airglow) to be obtained. Two-channel measurements using an FPI have been reported in some previous studies (Sica et al., 1986). Initially, these instruments were developed for local operation; automatic/remote control systems were added later. Thus, some redundancies exist in each system. For example, a separate PC is used for the automation system. However, these redundancies also enable the automatic control system to be independent of the main FPI system. Furthermore, operators can easily switch from the local observation mode to the remote mode, or *vice versa*.

We have developed two FPI systems that will be described in the next section.

These instruments will be installed in Poker Flat Research Range, Alaska, as part of a cooperative project with the Geophysical Institute, University of Alaska, Fairbanks. In most cases, the operator will be situated in Tokyo, Japan. To compensate for the difficulty in making frequent visits to the observatory, the automatic observation system contains multiple safety systems and current status displays.

In section II, the original systems of each optical instrument and their operation performance (for the observation of auroras) are described. Section III describes the FPI-34AUT automatic/remote control system. In section IV, we introduce the analysis software used to calculate the wind velocity and temperature from the observed fringe image. The last section presents a brief conclusion and the future prospects of these automated systems.

2. Optical system and their performances

Our optical system was initially introduced by Ishii *et al.* (1997), but it is worth describing the present system here because some improvements have been made since Ishii's paper was published. These instruments have already been used for some studies (Ishii *et al.*, 1999; Kosch *et al.*, 2000a, b). We have developed two types of FPIs. One is a conventional FPI that can scan the sky with a narrow field of view (1.4 degrees, full angle). This FPI can be directed towards the desired portion of the sky using a moving mirror system. The other FPI has a wide field of view (140 degrees, full angle); it can be used to obtain two-dimensional observations of the emissions. The two instruments are identical, except for their fore-optical systems. The core of each FPI is a 116 mm clear aperture, capacitance-stabilized Fabry-Perot etalon (Queensgate Instruments, Ltd., U.K.). The nominal etalon gap is 20.49 mm, corresponding to a free spectral range (FSR) of 9.766×10^{-12} m at 630.0 nm. The gap can be piezoelectrically scanned. The reflectivity of the inner surface of the etalon (R) is $90 \pm 2.5\%$ in the wavelength region between 557.7 nm and 850.0 nm (theoretical finess: 29.8). Figure 1(a) shows schematic diagrams of the scanning FPI and the all-sky FPI. The beam passing through the etalon is separated by a dichroic mirror that reflects emissions longer than 600 nm and allows shorter wavelength emissions to pass through. With this mirror and the interference filters, emissions at two different wavelengths can be simultaneously observed: one at 557.7 nm and the other at either 630.0, 843.0 or 850.5 nm. The wavelength of peak transmission and the full-width at half-maximum (FWHM) values of these filters are given in Table 1.

System calibration using lasers is often required during observations. To save time and labor during calibration with automatic observation systems, the laser fringes for the two channels are simultaneously obtained. Two kinds of laser tubes are used for the calibration; a He-Ne green laser for the shorter wavelength (wavelength: 543.5 nm; 05LGR025, Melles Griot Ltd.), and a He-Ne red laser is used for the longer wavelength (wavelength; 632.7 nm; 117A-1, Spectra Physics Ltd.). Figure 1(b) shows a schematic diagram of the simultaneous calibration. These laser emissions are merged with a fiber optics bundle (FBC-2-2-5-B, Fujikura Ltd.) and simultaneously untroduced into the instrument. Figures 2(a) and (b) are examples of calibrated laser fringes that have been obtained simultaneously (integration time: 5 min 33 s). The absence of emission
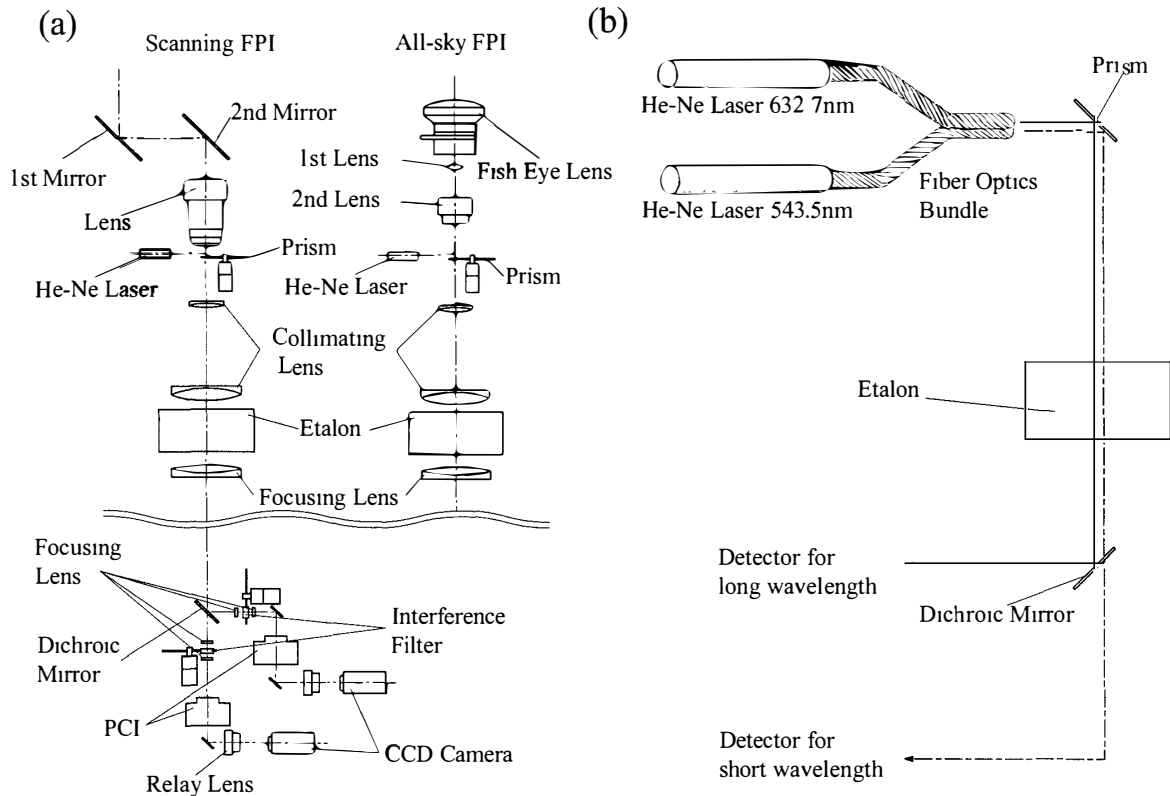
Fig. 1. (a) Schematic diagrams of Fabry-Perot interferometers developed at the Communications Research Laboratory; leftside of foreoptics: scanning Fabry-Perot interferometer, rightside of foreoptics: all-sky Fabry-Perot interferometer.

(b) Schematic diagram of two-channel simultaneous calibration: two different wavelengths of laser emissions are merged with fiber optics and transmitted to the etalon. The beam is split by a dichroic mirror, and fringe images of the two beams are produced.

Table 1. The center wavelength and the full width at half-maximum (FWHM) of the filters.

Scanning		All-sky	
Peak wavelength (nm)	FWHM (nm)	Peak wavelength (nm)	FWHM (nm)
557.521	2.0	557.700	1.9
630.841	2.7	630.664	2.6
843.034	1.0	843.134	1.0
850.496	1.0	850.636	1.1

contamination opposite lasers has been confirmed.

Photon Counting Imagers (PCIs, Hamamatsu Photonics Co., V5102UHX (S-20, S-25)) are employed to detect the fringes of weak emission. The PCI is a 3-stage proximity-focusing image intensifier with a phosphor screen output. The PCIs are cooled to $-15°C$ with a Peltier refrigerator to reduce thermal noise, and the heads are cooled by the circulation of water at a temperature of less than $+15°C$.

The enhanced fringe image is optically coupled to a CCD camera with a 512 by 480 pixels matrix. The video signal from the CCD camera is digitized with an A-D
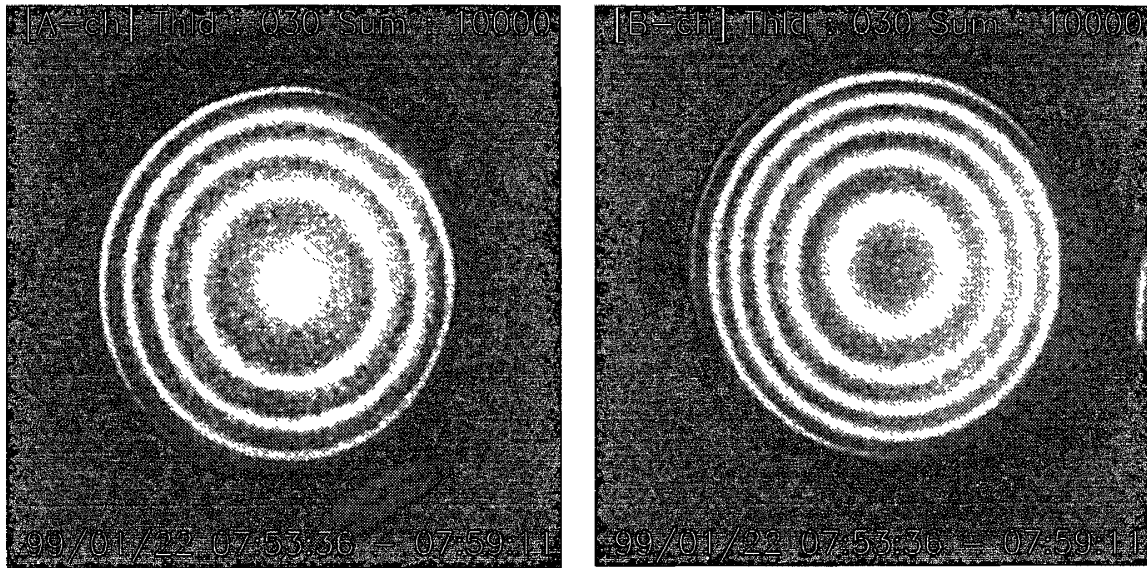
Fig. 2.   Examples of calibration fringes obtained with two different wavelength laser emissions:
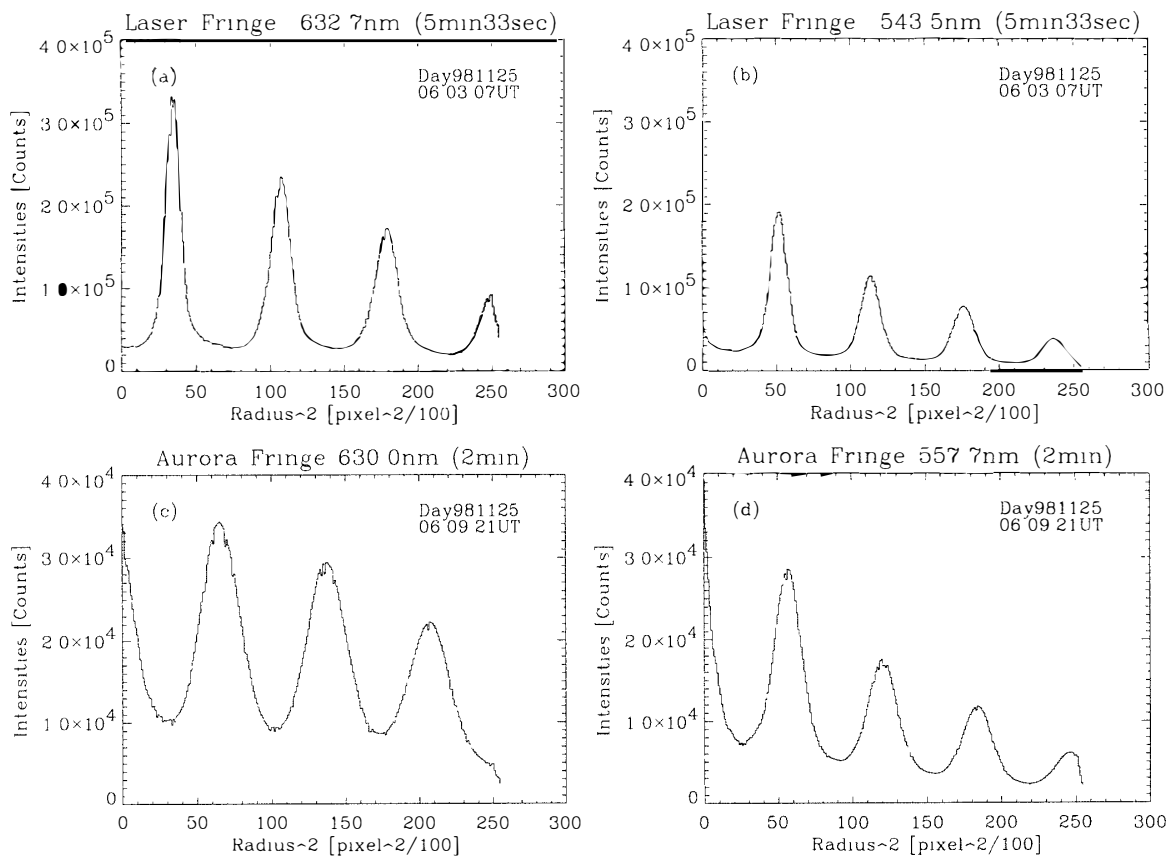(a) 632.7-nm He-Ne laser and (b) 543.5-nm He-Ne laser.

Fig. 3.   Cross sections of laser and aurora fringes.   (a) laser fringe (632.7 nm) with 5 min 33 s
exposure time, (b) laser fringe (543.5 nm) with 5 min 33 s exposure time, (c) aurora fringe
(630.0 nm) with 2 min exposure time, and (d) aurora fringe (557.7 nm) with 2 min
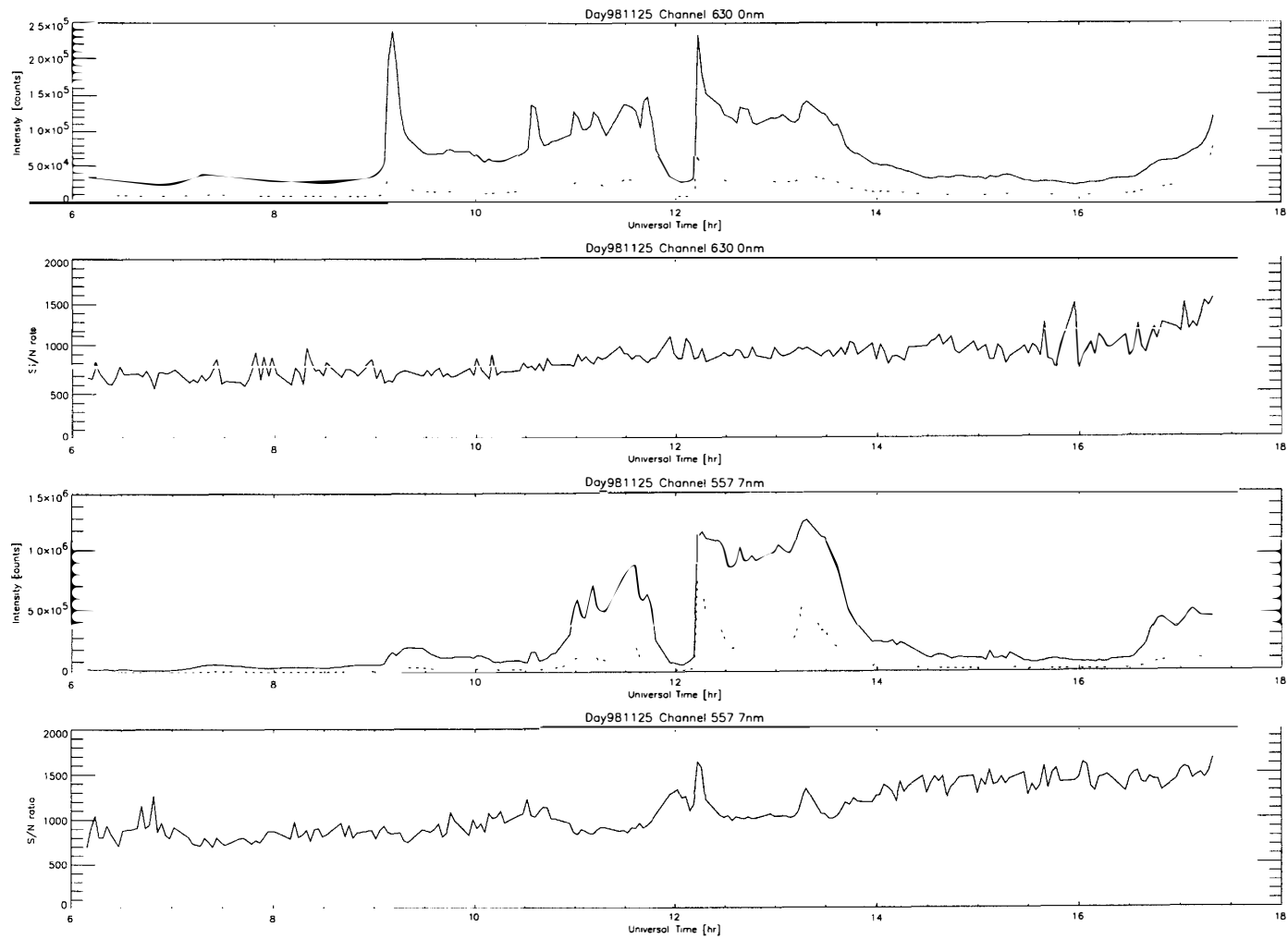exposure time.   The first two fringes were simultaneously obtained, as were the last two.

Fig. 4. Top and third panel: temporal variations in auroral intensity (solid line) and background level (dotted line) at 630.0 nm (top) and 557.7 nm (third). The intensities represent the number of photons counted at the first peak (auroral intensity) and the first bottom (background). Second and bottom panels: temporal variations in the S/N ratio. The definition of S/N ratio is described in the text

converter to reduce thermal noise from the PCI and CCD.   The digitized video images (30 frames/s) are accumulated in the image processor to produce an image with a good signal-to-noise ratio.   The accumulation time can be externally adjusted to the intensity of the incoming light.   In addition to the accumulation time, the transfer of data between the image processor and the computer and the software control of the image processor require about 10 s to save an image.   The exposure time for a high S/N ratio is 1–2 min for aurora and 5 min for airglow; thus, the required time to store the data is much shorter than the observation time.

   Figure 3 shows cross sections of the lasers ((a) and (b)) and observed aurora fringes ((c) and (d)).   Each fringe is obtained after summation in the azimuthal direction.   The center of fringes are determined from the center of the laser fringe measured on that particular night.   Figures 3a and 3b show the first-laser images obtained on Nov. 25, 1998, and Figs. 3c and 3d show the first observations obtained on that same date.   The condition of the aurora was quiet when these images were obtained (auroral luminosity was ~1 kR even at OI557.7 nm, which usually has an intensity of more than OI630.0 nm).   In spite of these weak aurora, the fringe shapes were not influenced by thermal noise.

Table 2.   Summary of the instrument parameters of the Fabry-Perot interferometers.

Parameter		Value		
Foreoptics				
Field of view	All-sky 140°		Scanning 1.4°	
Etalon (Queensgate Model ET116)				
Clear aperture		116 mm		
Reflectivity (at 557.7–850.0 nm)		0.90±0.025		
Theoretical reflective finesse		23.5–40.3		
Nominal optical spacing		20.49 mm		
PCI detector (Hamamatsu Model V5102UHX)(S-20, S-25)				
Collecting area		18 ϕ mm		
Resolution	S-20	20.21 line pairs/mm		
	S-25	25.41 line pairs/mm		
Amplification factor (photon counting mode)		10^7 fl/fc		
Quantum efficiency at 557.7 nm		10 %		
at 630.0 nm		11 %		
at 843.0 nm		4.7%		
at 850.5 nm		4.2%		
Dark count (0°)	S-20	8.2 cps/mm^2		
	S-25	4.1 cps/mm^2		
CCD detector (Hamamatsu C3077-02)				
Imaging area	H 8.8 mm		V 6.6 mm	
Pixel number	H 768		V 493	
Pixel size	H 11.0 μm		V 13.0 μm	

Figure 4 shows the temporal variations in the fringe peak and bottom intensities as well as the S/N ratio for the cross section of the fringes. The data set is the same as that used in Fig. 3 (Nov. 25, 1998). The solid and dotted line in the first and third panels show the intensities of the first peak and the first bottom of the fringes, respectively. The second and fourth panels show the S/N ratio of the fringes. These panels show that the SN ratio exceeds 500, even for weak aurora, with a 2 min exposure time. The other optical parameters are shown in Table 2.

One UNIX workstation is used to control the observation sequence and store the data images. Figure 5 shows a system diagram of the scanning FPI. The workstation also controls the stepping motors on the mirrors (for the scanning FPI only), the filter wheels, the prism turret for introducing the lasers, and the focusing lenses. In addition, the workstation sends commands to the image processor to integrate the video image and download the data to hard disk.

A few obstacles must be overcome to have fully automatic/remote control of these optical instruments. (1) Some devices, especially the PCIs, are very fragile, and any strong light (e.g., sunlight) can damage them. Thus, some kind of protection system is required. (2) The overall system contains independent electric devices. At the start of the observation period, some of these devices must be turned on sequentially. For instance, the water cooler and the dry air compressor should be turned on first; once the water temperature has decreased to ($\leq +15°C$), the PCI power should then be turned
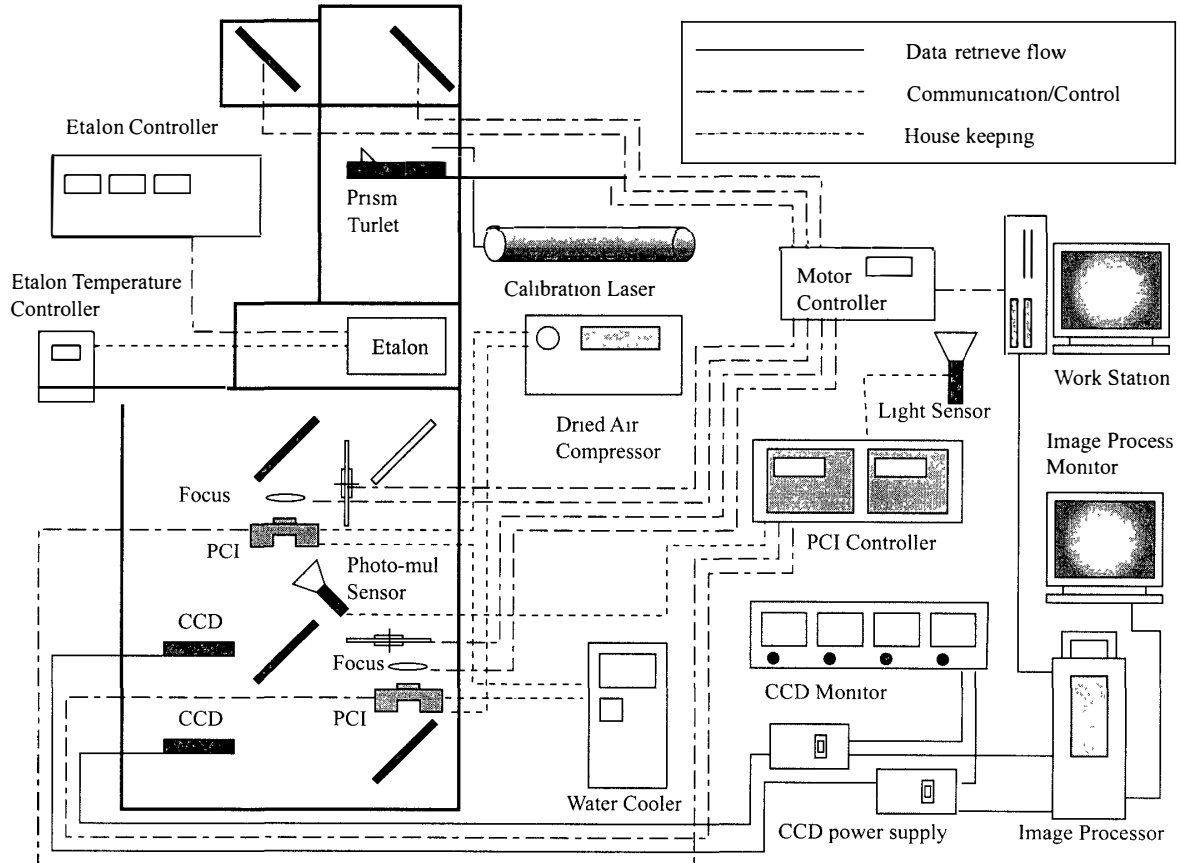

Fig. 5. System diagram of the optical control unit and the data retrieving unit.

on. (3) The full size of the fringe image data is large (~ half a mega byte for each image). Since the instruments can measure airglow/aurora emissions with a high temporal resolution (5 min 33 s for airglow, 1-2 min for aurora), a huge set of files is produced during an observation period. Consequently, the workstation requires a huge number of hard disks. The present system has an 8 G byte HD that has been partitioned. The automatic system must be able to assign the data sets to appropriate directories during the daytime.

3. Automatic observation system

The automatic observation system (FPI-34AUT, A.D. Inc.) consists of three parts: a main control box, a personal computer (PC, Fujitsu, FMV SIV165), and sensors. The system diagram for FPI-34AUT is shown in Fig. 6.

The start and end times of the observation period are controlled by the PC, and the observation schedule is written in a file named 'schedule.txt'. Read/write operations to this file can be performed from a remote site through the Internet or over a telephone line. Also, the present observation is shown in a file named 'status.txt' that can be accessed from any distant site.

The main control box contains the power supply switches for the dry air compressor, water cooler, calibration lasers, motor controller, CCD camera, PCI controller and
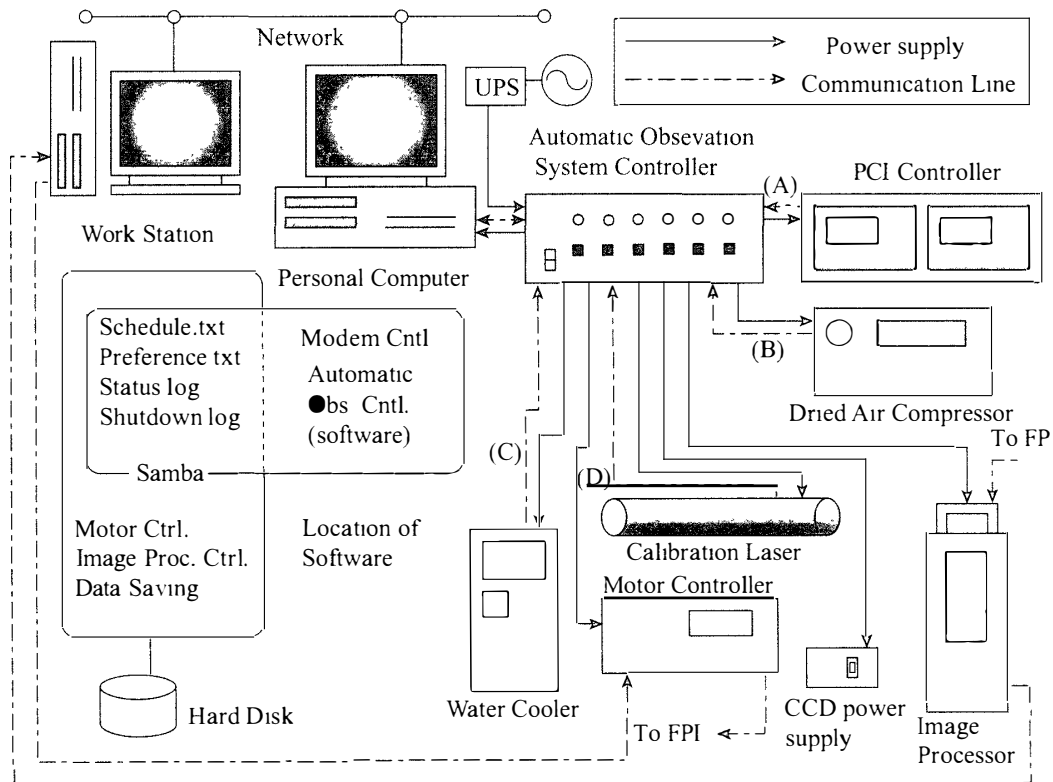

Fig. 6   System diagram of the automatic observation system (FPI-34AUT). The workstation, PCI controller, motor controller, CCD power supply and image processor shown in this figure are the same as that shown in Fig. 5.

image processor. When the start time arrives, the main box switches on the power to these instruments sequentially in the above order. The FPI-34AUT has sensors for monitoring the temperature and the flow of the cooling water as well as the flow of dry air. In addition, information on the stability of the He-Ne red laser frequency (wavelength 632.8 nm), the PCI head temperature, and the voltage from each controller is directly obtained. The PC checks these parameters and when they satisfy their criteria, the PC moves on to the next process. These criteria are defined in a setup file named 'preference.txt' on the PC; the operator can edit the file from a remote site even during observations.

Figure 6 shows the configuration of the software in the PC and workstation. The software for the automatic observation system is installed in the PC. The modem for communicating to the remote site is also connected to the PC. The software for the motor controller and image processor are installed in the workstation. The obtained fringe images are also saved on hard disks at the workstation. Some files containing information on the automatic observations are treated as common files for the PC and workstation using a software named 'Samba' (Blair, 1998). This system allows the PC and workstation to communicate reliably. The PC rewrites the common files every 10 s, and the workstation checks the files to determine the start/end of observations.

Once all the equipment is ready to perform the observations, the workstation receives information from the status file and starts the observation program. Finally, two important requirements must be satisfied before automatic FPI observations can be performed: fragile equipment, such as the PCI, must be protected from strong light, and the system must be protected against shutdowns in the electric power supply. For the former requirement, this system has two safety measures. The first is a gate circuit, which the original PCI controller also had. A photo-multiplier unit monitors the output intensity of the PCI and if the intensity exceeds the criterion, the unit stops the power supply to the PCI head for 10 s. After 10 s, the system checks the intensity once again and if the intensity still exceeds the criterion, the system repeats the process. This system guards against bright light emissions, which can occur quite suddenly. The other safety feature has a similar function but is not as sensitive. This sensor monitors the light levels outside the observatory and ensures that the power to the PCI controller is turned off during the day.

To guard against shutdowns in the electric power supply, our system has two UPS (Uninterruptible Power Supplys) systems: one for the workstation and the other for the FPI-34AUT. Short shutdowns do not pose a problem. The UPS maintains the supply of electricity to the dry air compressor, stabilization laser, PCI, CCD, image processor and PC. The water cooler and motor controller are not supported because they require a relatively high power supply and short interruptions in their operation (several minutes) are not critical. The FPI-34AUT ends the observation period if a relatively long shutdown occurs (≥ 10 min), and all electric devices except for the dry air compressor are stopped at the same time. The dry air compressor continues to function for 1 min after the shutdown to prevent moisture from condensing on the PCI heads.

The operator can change the parameters during observation period. For example, if the operator finds that the quality of the fringe images is poor, the gain of the PCI or the focus can be adjusted.

When the observations are completed, the FPI-34AUT rewrites the status file to the common directory and switches off all the equipment except for the dry air compressor. The dry air compressor continues to operate for 20 min after the end of the observation period. The workstation stops the observation period when it obtains an end signal from the status file and waits until the start time of the next observation period.

Observation data files are initially saved to a temporary directory on the workstation. The file management program starts with the "cron" system in UNIX (Sun OS 4.1.4) at noon. The program searches for available space on each disk and moves the files to a directory that has sufficient space.

4.   Determination of wind and temperature in the thermosphere

Figure 7 shows the software used to estimate temperature and wind velocity. The programs for the first two processes, the determination of the laser fringe's center and the calculation of the cross section for the 24 directions, are written with C language. The remainder of the programs are written with the IDL programming language (Interactive Display Language, version 5.1, Research System Inc.).

The most important part of the analysis is the fitting routine. We use two types of fitting routines; the first process is a Gaussian fitting to the laser fringe peaks and the second is a deconvolution of the observation fringe peaks with the instrument function. The former routine is used in part (a), and the latter one is used in part (b) of Fig. 7. The Gaussian fitting is important for estimating the shape of the laser fringes and the effect of the etalon gap drift. The distortion of a laser fringe is estimated from the spatial variations in the radius of the laser fringe in 24 directions. Observations of the fringe shapes are adjusted before superposing the cross sections in 24 directions. The etalon gap drift is estimated from the temporal variation in the radius of one laser fringe. The temporal drift of the fringe peak is ~1.5 pixels in 7 hours, corresponding to a velocity of ~100 m/s.

One laser image was obtained for every ten observations (every 20 min for aurora observations and every hour for airglow observations) to remove this artificial effect.

The Gaussian fitting routine was carefully selected to suit our uses. To examine the performance of the fitting programs, the programs were applied to simulated Gaussians that were numerically generated from precisely known values of the model parameters. Here, the fitting performance of the software used in part (a) is shown. The performance used in part (b) is not shown here because it was examined in Conde (2000). The fitting program in part (a) uses a gradient-expansion algorithm to compute a non-linear least squares fit to the Gaussian function with four parameters: peak position, peak height, peak width and background level. Iterations are performed until the χ-square changes by a specified amount (1.0×10^{-3}) or until a maximum number of iterations ($=20$) have been performed.

The peak height of the simulated Gaussian is randomly selected from between 72 and 3600. This height corresponds to a 2-min observation of an aurora with various luminosities. The amplitude of the thermal noise is fixed at 100, which is a typical value for our instruments. The position and width of the peak position are given as 54 and 5, respectively. The statistical distribution of results that fit these parameters is then
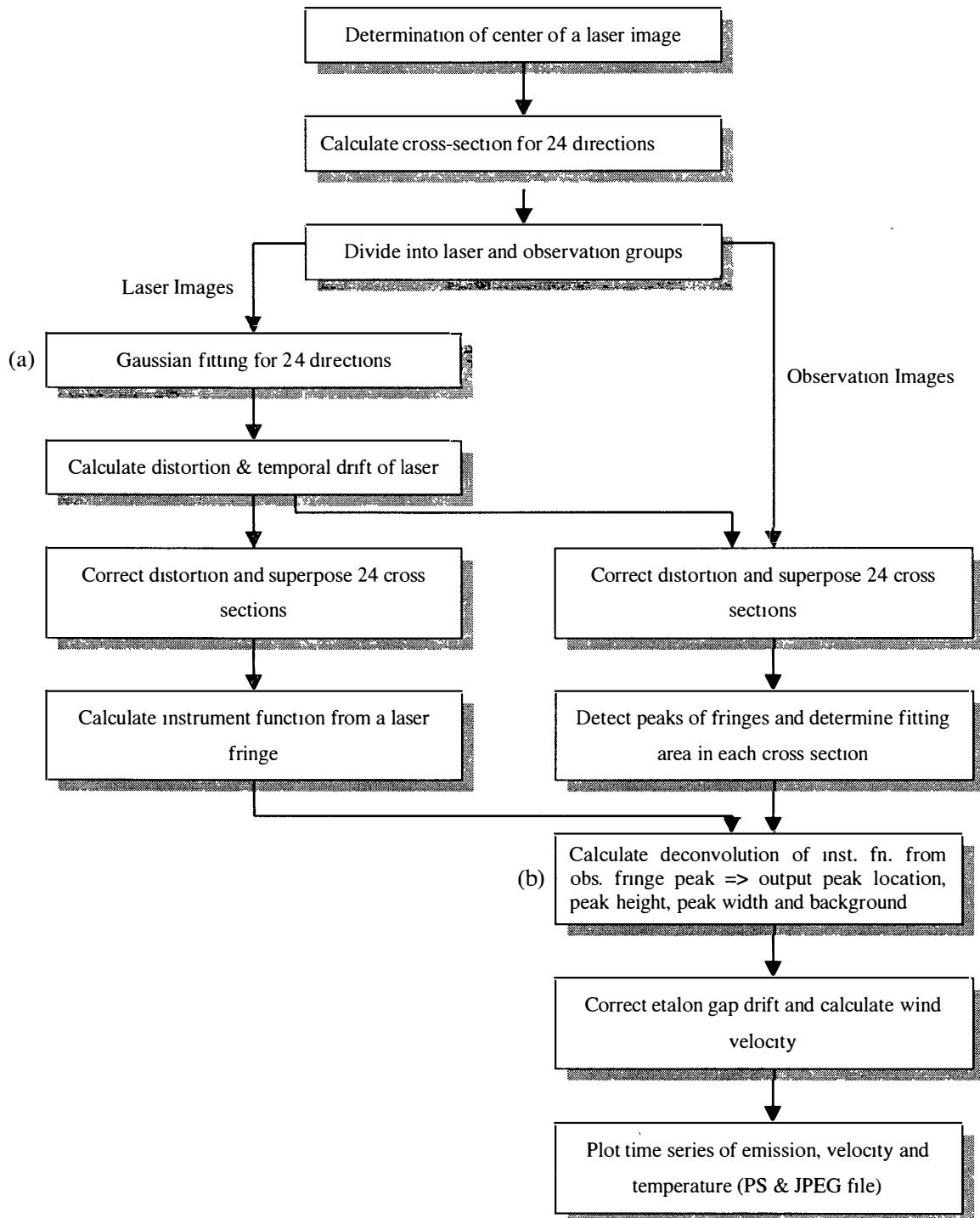
Fig. 7. Analysis procedure for estimating physical parameters from row fringe data.

considered for a large (10000 elements) set of simulated Gaussians.   Figure 8 shows the calculated error values versus the peak count rate.   The peak count rate means the ratio between the actual peak height and the maximum height ($=3600$).

We used a scheme described by Conde (2000) to determine the peak and background emission, the peak position and the temperature of the neutral emission layer. The instrument function is generated by taking the cross section of the laser fringe
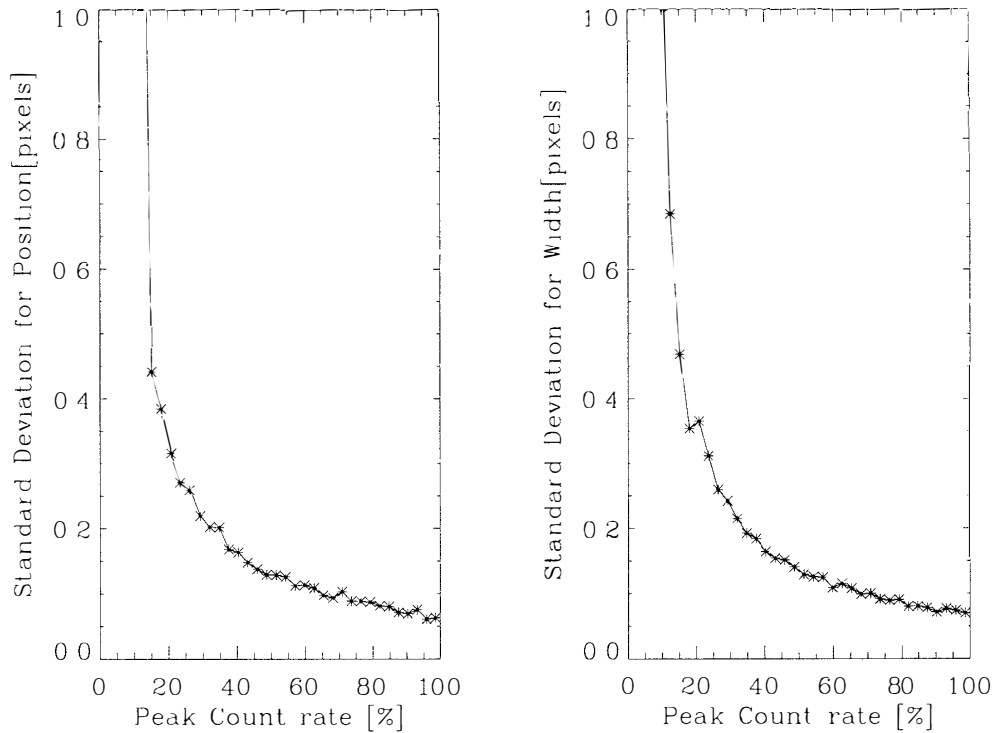
Fig. 8.   *Calculated error values versus peak count rate for determining the peak position and width.*
The peak height of the simulated Gaussian is randomly assigned a value between 72 and
3600; the amplitude of the random noise is fixed at 100.   The statistical distributions of fit
results are considered for a 10000 element set of simulated Gaussians.   The peak count
rate represents the ratio between the actual peak count and the maximum count (=3600).

obtained at the first calibration.   The scheme of Conde (2000) was designed for the
analysis of backscatter spectra recorded during an atmospheric Doppler lidar experi-
ment and calculates five parameters: temperature, Doppler shift, molecular and aerosol
peaks and background.   Since we do not need information regarding aerosol peak, this
value is fixed.

The typical error estimates for the wind velocity and temperature in the OI 630.0
nm fringe image using the above program are $\sim \pm 5$ m/s and ± 20 K, respectively.

5.   Concluding remarks and future prospects

We have developed a scanning and an all-sky FPI that utilize an automatic
observation system.   This new system makes it possible to control fragile optical
instruments from a remote location.   A personal computer controls the observation
period; when the observation period begins, the system switches on the equipment in a
pre-fixed order.   Certain sensors monitor the system conditions, such as the cooling
water temperature, the flow of water and air, and the temperature and voltage of the
detectors.   Two protection systems have been installed to prevent damage to the fragile
detector

We have also developed a new analysis code to estimate the emission intensity,
line-of-sight wind velocity and temperature.   Compared with the performance of our

previous version, the precision of these parameters has been considerably improved. We examined the performance of three Gaussian fitting programs and selected the best one for our use. The program described in Conde (2000) was used to estimate these physical parameters. The effect of the etalon gap drift was removed using laser calibration data.

Since the automatic observation system was added to an already existing optical system, the total system has some areas of redundancy. If necessary, a more compact version of this system could be established. In addition, cable communication (Internet or telephone line) is presently used to communicate with the system from a remote location. Once the system is modified for radio communication, a relocatable optical observatory will become possible, representing a remarkable evolution in optical observation technology.

Acknowledgments

References

Aruliah, A.L. and Rees, D. (1995): The trouble with thermospheric vertical winds: geomagnetic, seasonal and solar cycle dependence at high latitudes. J. Atmos. Terr. Phys., **57**, 597–609.

Babcock, H.D. (1923): A study of the green auroral line by the interference method. Astrophys. J., **57**, 209–221.

Batten, S., Rees, D., Wade, D. and Steen, A. (1988): Observations of thermospheric neutral winds by the UCL Doppler imaging system at Kiruna in northern Scandinavia. J. Atmos. Terr. Phys., **50**, 861–888.

Biondi, M.A., Meriwether, J.W., Jr., Fejer, B. and Woodman, R. (1988): Measurements of the dynamics and coupling of the equatorial thermosphere and the F-region ionosphere in Peru. J. Atmos. Terr. Phys., **50**, 937–942.

Biondi, M.A., Sipler, D.P., Zipf, M.E. and Baumgardner, J.L. (1995): All-sky Doppler interferometer for thermospheric dynamics studies. Appl. Opt., **34**, 1646–1654.

Blair, J.D. (1998): Samba, integrating UNIX and Windows, Specialized Systems Consultants.

Buonsanto, M.J., Tung, Y.-K. and Sipler, D.P. (1992): Neutral atomic oxygen density from nighttime radar and optical wind measurements at Millstone Hill. J. Geophys. Res., **97**, 8673–8679.

Burnside, R.G., Herrero, F.A., Meriwether, J.W., Jr. and Walker, J.C.G. (1981): Optical observations of thermospheric dynamics at Arecibo. J. Geophys. Res., **86**, 5532–5540.

Conde, M. (2000): Analysis of Fabry-Perot spectra of lidar backscatter echoes. ANARE Res. Notes (in press).

Conde, M. and Smith, R.W. (1998): Spatial structure in the thermospheric horizontal wind above Poker Flat, Alaska, during solar minimum. J. Geophys. Res., **103**, 9449–9471.

Crickmore, R.I., Dudeney, J.R. and Rodger, A.S. (1991): Vertical thermospheric winds at the equatorward edge of the auroral oval. J. Atmos. Terr. Phys., **53**, 485–492.

Fabry, C. and Perot, A. (1896): Mesure de petites epaisseurs en valeur absolue. Compt. Rend., **123**, 802–805.

Fabry, C. and Perot, A. (1897): Sur les franges des lames minces argentees et leur application a la mesure de

petites epasseurs d'air. Ann. Chim. Phys. **12**, 459–501.

Hays, P.B., Killeen, T.L., Spencer, N.W., Wharton, E., Roble, R.G., Emery, B.A., Fuller-Rowell, T.J., Rees, D., Frank, L.A. and Craven, J.D. (1984): Observations of the dynamics of the polar thermosphere. J. Geophys. Res., **89**, 5597–5612.

Hernandez, G. (1982): Mid-latitude thermospheric neutral kinetic temperatures 1. Solar, geomagnetic, and long-term effects. J. Geophys. Res., **87**, 1623–1632.

Innis, J.L., Greet, P.A. and Dyson, P.L. (1996): Fabry-Perot spectrometer observations of the auroral oval/polar cap boundary above Mawson, Antarctica. J. Atmos. Terr. Phys., **58**, 1973–1988.

Innis, J.L., Dyson, P.L. and Greet, P.A. (1997): Further observations of the thermospheric vertical wind at the auroral oval/polar cap boundary above Mawson station, Antarctica. J. Atmos. Terr. Phys., **59**, 2009–2022.

Ishii, M., Okano, S., Sagawa, E., Watari, S., Mori, H., Iwamoto, I. and Murayama, Y. (1997): Development of Fabry-Perot interferometers for airglow observations. Proc. NIPR Symp. Upper Atmos. Phys., **10**, 97–108.

Ishii, M., Oyama, S., Nozawa, S., Fujii, R., Sagawa, E., Watari, S. and Shinagawa, H. (1999): Dynamics of neutral wind in the polar region observed with two Fabry-Perot Interferometers. Earth Planets Space, **51**, 833–844.

Killeen, T.L. and Roble, R.G. (1988): Thermosphere dynamics: Contributions from the first 5 years of the Dynamics Explorer program. Rev. Geophys., **26**, 329–367.

Killeen, T.L., Craven, J.D., Frank, L.A., Ponthieu, J.J., Spencer, N.W., Heelis, R.A., Brace, L.H., Roble, R.G., Hays, P.B. and Carignan, G.R. (1988): On the relationship between dynamics of the polar thermosphere and morphology of the aurora: Global-scale observations from Dynamics Explorers 1 and 2. J. Geophys. Res., **93**, 2675–2692.

Kosch, M.J., Ishii, M., Nozawa, S., Rees, D., Cierpka, K., Kohsiek, A., Schlegel, K., Fujii, R., Hargfors, T, Fuller-Rowell, T.J. and Lathuillere, C. (2000a): A comparison of thermospheric winds and temperatures from Fabry-Perot interferometer and EISCAT radar measurements with models. Adv. Space Res., **26**, 979–984.

Kosch, M.J., Ishii, M., Kohsiek, A., Rees, D., Schlegel, K., Hagfors, T. and Cierpka, K. (2000b): A comparison of vertical thermospheric winds from Fabry-Perot interferometer measurements over a 50 km baseline. Adv. Space Res., **26**, 985–988.

Meriwether, J.W., Jr., Tepley, C.A., Price, S.A., Hays, P.B. and Cogger, L.L. (1983): Remote ground-based observations of terrestrial airglow emissions and thermospheric dynamics at Calgary, Alberta, Canada. Opt. Eng., **22**, 128–131.

Meriwether, J.W., Jr., Moody, J.W., Biondi, M.A. and Roble, R.G. (1986): Optical interferometric measurements of nighttime equatorial thermospheric winds at Arequipa, Peru. J. Geophys. Res, **91**, 5557–5566.

Nakajima, H., Okano, S., Fukunishi, H. and Ono, T. (1995): Observations of thermospheric wind velocities and temperatures by use of a Fabry-Perot Doppler imaging system at Syowa Station, Antarctica. App. Opt., **34**, 8382–8395.

Rees, D. and Greenaway, A.H. (1983): Doppler imaging system; an optical device for measuring vector winds, 1, General principles. App. Opt., **22**, 1078–1083.

Rees, D., Greenaway, A.H., Gordon, R., McWhirter, I., Charleton, P.J. and Steen, A. (1984): The Doppler imaging system: initial observations of the auroral thermosphere. Planet. Space Sci., **32**, 273–285.

Sica, R.J., Rees, M.H., Romick, G.J., Hernandez, G. and Roble, R.G. (1986): Auroral zone thermospheric dynamics, 1. Averages. J. Geophys. Res., **91**, 3231–3244.

Sipler, D.P., Biondi, M.A. and Roble, R.G. (1983): *F*-region neutral winds and temperatures at equatorial latitudes: measured and predicted behaviour during geomagnetically quiet conditions. Planet. Space Sci., **31**, 53–66.

Smith, R.W. and Hernandez, G. (1995): Vertical winds in the thermosphere within the polar cap. J. Atmos. Terr. Phys., **57**, 611–620.

Walterscheid, R.L., Lyons, L.R. and Taylor, K.E. (1985): The perturbed neutral circulation in the vicinity of a symmetric stable auroral arc. J. Geophys. Res., **90**, 12235–12248.